Nat. Hazards Earth Syst. Sci., 16, 1269–1288, 2016
www.nat-hazards-earth-syst-sci.net/16/1269/2016/
doi:10.5194/nhess-16-1269-2016

Natural Hazards and Earth System Sciences
Open Access
EGU

Quantification and analysis of geomorphic processes on a recultivated iron ore mine on the Italian island of Elba using long-term ground-based lidar and photogrammetric SfM data by a UAV

Florian Haas[1], Ludwig Hilger[1], Fabian Neugirg[1], Kathrin Umstädter[1], Christian Breitung[1], Peter Fischer[2], Paula Hilger[1,a], Tobias Heckmann[1], Jana Dusik[1], Andreas Kaiser[3], Jürgen Schmidt[3], Marta Della Seta[4], Ruben Rosenkranz[4,b], and Michael Becht[1]

[1]Chair of Physical Geography, Catholic University of Eichstätt-Ingolstadt, 85072 Eichstätt, Germany
[2]Applied Physical Geography, Catholic University of Eichstätt-Ingolstadt, 85072 Eichstätt, Germany
[3]Soil and Water Conservation Unit, Technical University Bergakademie Freiberg, 09599 Freiberg, Germany
[4]Dipartimento di Scienze della Terra, Universitá degli Studi di Roma "La Sapienza", 00185 Rome, Italy
[a]now at: Geological survey of Norway NGU, 7040 Trondheim, Norway
[b]now at: University of Bremen, Department of Geosciences, 28359 Bremen, Germany

Correspondence to: Florian Haas (florian.haas@ku.de)

Received: 21 September 2015 – Published in Nat. Hazards Earth Syst. Sci. Discuss.: 13 October 2015
Revised: 28 April 2016 – Accepted: 3 May 2016 – Published: 31 May 2016

Abstract. This study focuses on the quantification and analysis of geomorphic processes on the barely vegetated slopes of a recultivated iron ore mine on the Italian island of Elba using photographs from terrestrial laser scanning (TLS) and digital photogrammetry by an unmanned aerial vehicle (UAV) over a period of 5 1/2 years. Beside this, the study tried to work out the potential and the limitations of both methods to detect surface changes by geomorphic process dynamics within a natural environment. Both UAV and TLS show the pattern of the erosion and accumulation processes on the investigated slope quite well, but the calculated amounts differ clearly between the methods. The reasons for these differences could be found in the different accuracies (variable level of detections) of the methods and the different viewing geometries. Both effects have an impact on the detectable process dynamics over different timescales on the slope and their calculated amounts, which in both cases can lead to an underestimation of erosion and accumulation by fluvial processes.

1 Introduction

Fluvial erosion plays a major role in the geomorphic formation of steep slopes (Bryan, 2000) in agricultural (Diodato and Bellocchi, 2000; Auerswald et al., 2000) as well as in natural landscapes of the Alps (Wetzel, 1992; Haas, 2008) or the Mediterranean region (Clarke and Rendell, 2006; Mathys et al., 2005). Especially in the Mediterranean regions, the climatic conditions in combination with the topography and the lithology lead to intensive gullying and bad land generation (Della Seta et al., 2009; Aucelli et al., 2012), with high intensities on steep and barely vegetated slopes (Haas et al., 2011). The geomorphic process dynamic, including hazards, can be intensified by anthropogenic influences, such as deforestation for agricultural utilization (Aucelli et al., 2012) or major changes e.g., by mining (Nowotny, 2003; Martín-Duque et al., 2010; Mossa and James, 2013). Especially mining sites in hilly or mountainous regions can show steep and mostly anthropogenically created slopes (also due to a recultivation) without natural soils and changed hydrological conditions influencing surface hydrology, flow paths, and groundwater level (Osterkamp and Joseph, 2000). In the case of former iron ore exploitation, the leftover spoil often consists of

heavy metal polluted sediments with harsh conditions for stabilizing vegetation. Thus in combination with heavy rainfall, the slopes are often prone to erosion processes. Due to the rapid change of topography, such nonequilibrium landscapes (Hancock et al., 2008) can also provide sediments for subsequent geomorphic processes (e.g., mass movements or debris flows) and furthermore act as a source of heavy metal pollutants (Servida et al., 2009; Benvenuti et al., 1999) influencing e.g., the quality of drinking water. Investigations of the geomorphic process dynamic in this environment is thus of major importance for society, as they can show both potentially vulnerable areas or the success of recultivation projects. Beside the societal relevance, anthropogenically formed landscapes are interesting objects for the studies of geomorphic processes. As recultivated landscapes were set back, geomorphic processes start at "time zero" and thus can be analyzed ab initio (cf. Hancock et al., 2008).

The investigation of geomorphic processes, e.g., fluvial erosion on hilly or mountainous slopes in Mediterranean regions, was often done by using analog methods like erosion pins or sediment traps (Della Seta et al., 2009; Haas et al., 2011; Clarke and Rendell, 2006); but they are often hard to use and error-prone, as their use can lead to other influences on the investigated slopes (Haas et al., 2011). Moreover, the spatial and temporal resolution of these methods is normally very limited with consequences for the interpretation of the results (Haas et al., 2011). Digital geodetic methods like terrestrial laser scanning (TLS), also known as ground-based lidar and digital photogrammetry (or structure from motion – SfM), are increasingly being used for geoscientific research (c.f. Abellán et al., 2009; Schürch et al., 2011; Haas et al., 2012; d'Oleire-Oltmanns et al., 2012; Ouédraogo et al., 2014; Peter et al., 2014; Prosdocimi et al., 2015), as for the measurement of fluvial erosion or gullying on slopes of the Mediterranean region (Haas et al., 2011; d'Oleire-Oltmanns et al., 2012; Peter et al., 2014; Neugirg et al.; 2014) or on mining sites (cf. Hancock et al., 2008, 2015; Chen et al., 2015; Francioni et al., 2015). Beside these works, Tarolli (2014) gives a very detailed review of the applicability of the methods for the understanding of earth surface processes. Many of the studies include investigations about the accuracy of the single methods (Ouédraogo et al., 2014; James and Robson, 2012; Fonstad et al., 2013; Kaiser et al., 2014; Prosdocimi et al., 2015) but there are only a few studies that compare SfM by an unmanned aerial vehicle (UAV) and TLS to each other (Eltner et al., 2015; Flener et al., 2013; Sperlich et al., 2014) or the potential of both methods (especially UAV with its preferred bird's-eye viewing angle) for the detection of geomorphic processes in a natural environment by using long-term multitemporal data (Smith and Vericat, 2015).

Thus the presented work focuses on the use of TLS and SfM by UAV photographs to quantify and to analyze the geomorphic process dynamics on an artificial, steep, and sparsely vegetated slope of a former iron ore mine on the Mediterranean island Elba in Italy over 5 1/2 years. Beside the quantification and analysis of the erosion processes, an additional focus was set on the comparison of both methods and the identification of their potential and limitations for long-term monitoring of surface change by geomorphic activity in an artificial environment.

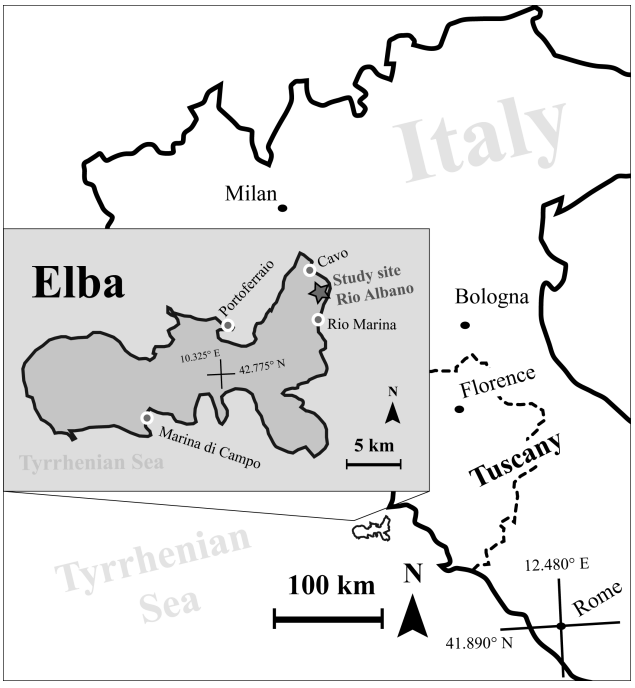

Figure 1. Location of the study area.

2 Study area

The studied slope is part of the former iron ore mine Rio Albano (haematite and pyrite) close to Rio Marina and Cavo on the east coast of the island of Elba, which is located close to the western coast of Italy (see Fig. 1). Elba is known as one of the most important mining sites of Italy, but the iron exploitation at Rio Marina ceased in 1981 (Servida et al., 2009) and left many waste dumps that are prone to erosion and therefore act as a potential source of sediments and heavy metal pollutants (Benvenuti et al., 1999; Mascaro et al., 2001). Especially the topographic structure of the mine with steep, unconsolidated and thus erosion-prone slopes in a short distance to the coast (polluted water is flowing directly into the sea) or to infrastructure (main roads are threatened e.g., by debris flows) has led to a variety of restoration projects on these waste dumps in order to minimize or stop the export of harmful substances (Servida et al., 2009) and sediments.

Figure 2 indicates that the mine surface is only barely vegetated, which is a consequence of the heavy metal concentration of the sediment and the very acidic soil and soil water conditions. Servida et al. (2009) measured pH values of 2.08 to 3.35 and very high heavy metal concentrations (e.g.,

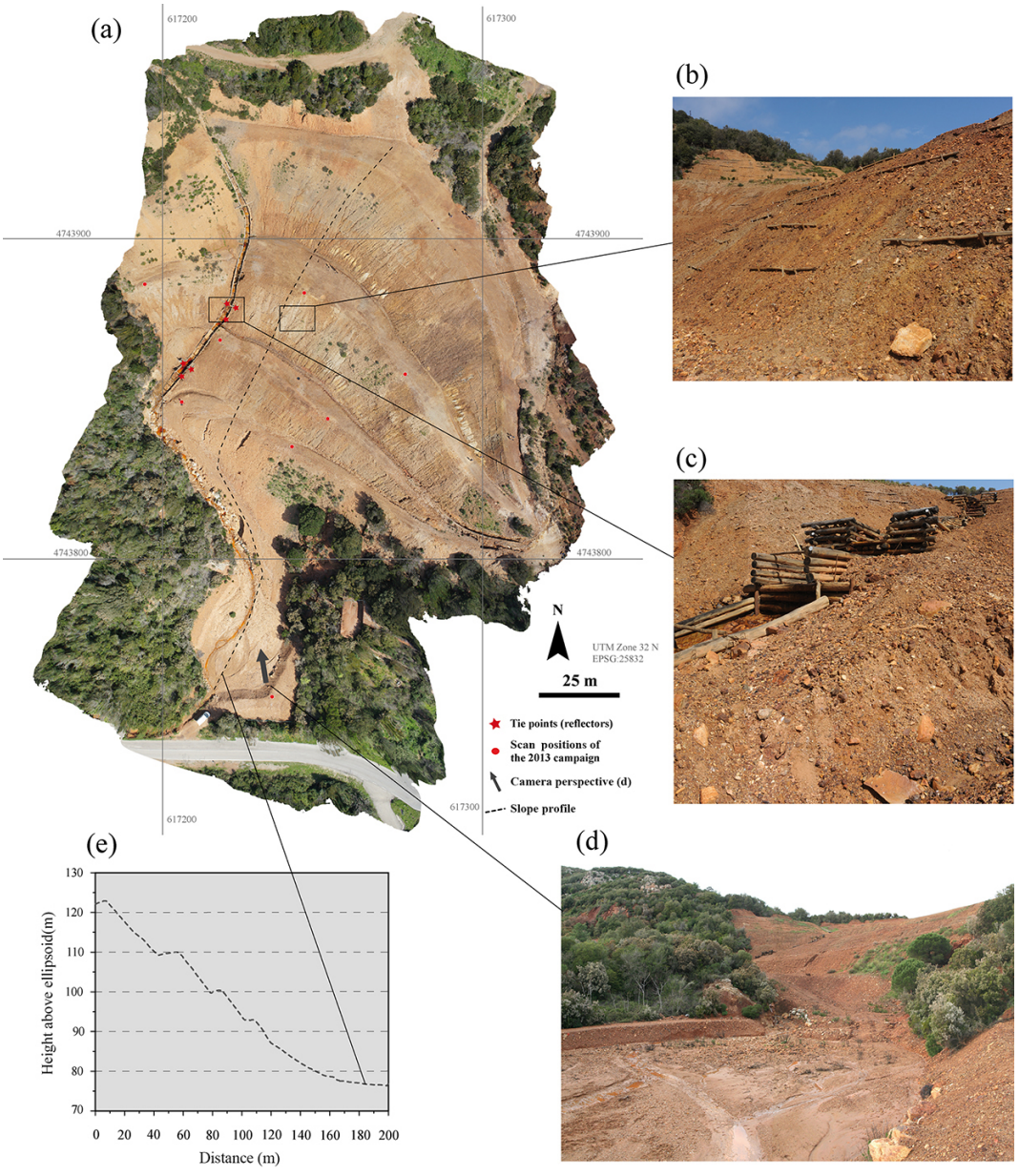

Figure 2. (a) Orthorectified and referenced aerial photograph (by the 2013 UAV campaign, ground resolution 5 cm) of the investigated slope with the 2013 scanning positions, **(b)** the artificial barriers on the slope, **(c)** a part of the main artificial drainage channel, **(d)** photograph of the slope and part of the reservoir, and **(e)** profiles of the artificial slope and the main artificial drainage channel.

903.16 mg L^{-1} for Fe). This is a decisive disadvantage for any restoration attempts by e.g., reforestation. As a stabilization of the slope by vegetation is not feasible, the slope was artificially benched in 2002 in order to reduce the flow velocities and thus minimize the erosion by water (Fig. 2e). Additionally, several artificial barriers were put directly on the slope for erosion control (Fig. 2b), but many of them were swept away as a result of erosion processes during recent years.

The overland flow from the single short slopes is collected by constructed channels at the foot of the slopes, which drain to a main drainage channel (Fig. 2c). On the end of the constructed channel, a low channel slope gradient causes deposition of the transported sediments in a reservoir before the water leaves the mine.

The mainly southernly exposed slope with a height difference of 47.8 m (heights lie between 76.2 and 124.0 m above ellipsoid) has an extension of 13 800 m^2 (including 1100 m^2 accumulation area) and consists of mainly coarse-grained (> sand) mine filling material and slag (Neugirg et al., 2016). The slope angles range from 14 to 69° with a mean of 39°.

Table 1. Information about all TLS epochs

TLS campaign	Scan positions	Number of total points (unfiltered)	Number of total points (filtered)	Mean point density per 0.01 m^2 (σ)/ m^{-2} (σ) (filtered data)	3-D error of global reg. (m)	σ of the MSA reg. for scans of one time step (m)
Sep 2009	7	18 943 687	3 780 803	3.6 (1.9)/288.1 (165.5)		0.009–0.013
Apr 2012	11	46 542 218	5 386 857	4.7 (2.0)/408.1 (182.6)		0.007–0.011
Apr 2013	9	39 082 545	4 087 117	4.1 (2.1)/330.2 (185.5)	0.015	0.008–0.012
Apr 2014	8	31 984 062	4 192 532	4.2 (2.0)/342.6 (177.5)		0.008–0.011
Apr 2015	9	44 062 211	5 278 825	4.7 (2.1)/396.3 (195.3)		0.009–0.011

The climatic conditions of the region are characterized by a mean annual rainfall of around 750 mm (for Populonia, which is located on the Italian mainland close to Elba), with main precipitation occurring during the winter period (83 % of rainfall between September and April) and a mean annual temperature of 15.3 °C (Giusti, 1993).

3 Materials and methods

3.1 Field campaigns and data acquisition

The investigation started in September 2009 with the first scanning of the whole slope. Since 2009, four more scanning campaigns have followed; these took place between April 2012 and April 2015 in order to quantify the erosion processes and are now additionally embedded in a DFG-founded project (German Science Foundation/HA 5741/3-1 and SCHM 1373/8-1). As the scanning of the very complex slope is very time-consuming, and in order to test the applicability of SfM by UAV photographs, the slope was additionally surveyed with aerial photographs by a UAV during two campaigns in April 2013 and April 2015.

3.1.1 Terrestrial laser scanning

Terrestrial laser scan data were acquired using the Riegl LMS Z420i scanner (http://www.riegl.com), which has a maximum measurement range up to 1000 m, an accuracy of 0.01 m (distance by single shot), and a scanning rate of up to 8000 pts s^{-1}. The scanner uses a near-infrared laser signal by a beam divergence of 0.25 mrad, which means an increase of the laser footprint by 0.0025 m per 100 m. A mounted digital SLR camera (Nikon D700 with a 20 mm lens) takes referenced high-resolution pictures of the scanned objects, in order to define the color (RGB value) of every single point of the lidar point cloud. This color information is applicable for manual or automatic filtering of vegetation (Haas et al., 2011). The scanner and the SLR camera are operated by an external PC and the scanner software RiscanPro (3-D scanner software).

The mine was scanned from between 7 (2009) and 11 (2012) different scan positions (Table 1) in order to minimize shadowing effects. The angular scanning resolution was set to 0.05° (x and y direction). Figure 2a shows as an example the location of the single scan positions of the 2013 campaign. For an accurate referencing of the point clouds, six fixed and stable tie points were installed on or near the slopes (reflector disks with a diameter of 0.1 m). These were mounted with screws or nails on the wooden debris flow barrier (see Fig. 3). This wooden debris flow barrier is the only stable construction on and around the slope, where a mounting of tie points was possible. The global coordinates of these tie points were measured using a differential GPS and a total station (Sect. 3.2).

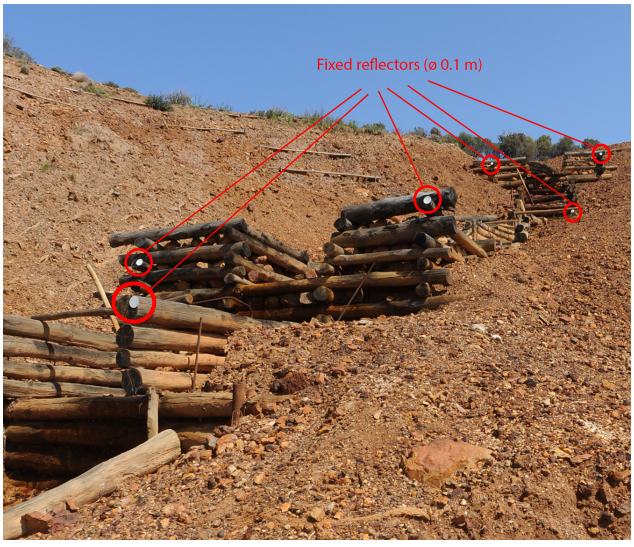

Figure 3. Picture of the mounted tie points on the debris flow barrier.

Following the data acquisition in the field, the software RiscanPro was used for the post-processing of the raw data (see Fig. 5). The single point clouds of each time step were registered globally using the scanned tie points. All scan positions of each single scanning epoch were referenced to one master scan which provided these global coordinates. All other scan positions were well distributed over the slope in order to ensure enough overlap of the single point clouds for

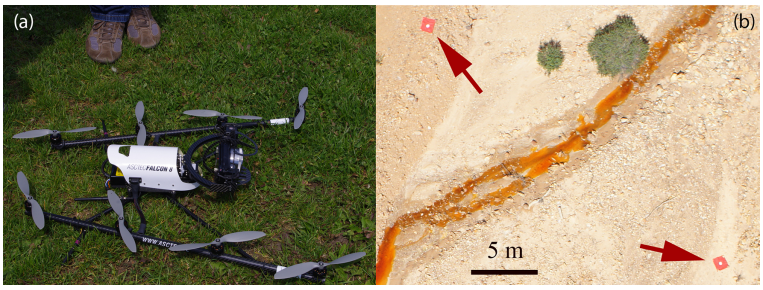

Figure 4. **(a)** The Astec Falcon 8 UAV and **(b)** carpets with reflectors used as GCPs for exterior orientation.

Table 2. Information about both UAV epochs.

UAV campaign	Number of pictures	Number of tie points for exterior orientation	Number of total points (unfiltered)	Number of total points (filtered)	Mean point density per 0.01 m^2 (σ)/ m^{-2} (σ) (filtered data)	Error of the exterior orientation (m)
Apr 2013	48	31	19 275 220	6 043 475	4.5(1.4)/418.2(114.6)	0.034
Apr 2015	158	37	60 016 606	5 925 190	4.5 (1.4)/418.2 (114.6)	0.048

the subsequent referencing procedure using an ICP-based algorithm (MSA tool in RiscanPro). The values for the referencing precision lie between 0.007 and 0.013 m. Table 1 shows the number of the scan positions on the slope, the referencing precision as mean value, the resulting number of points, and the point density (points m^{-2}) for every single epoch.

After these processing steps in RiscanPro the resulting raw point clouds were ASCII-formatted (x, y, z, RGB values) and exported as global coordinates. All further processing steps (e.g., filtering of vegetation, digital elevation model (DEM) generation) were done by using LIS Desktop/SAGA geographical information system (GIS) (www.laserdata.at, Sect. 3.2).

3.1.2 UAV survey – photogrammetry

During the campaign in April 2013 and April 2015 the Rio Marina mining area was additionally monitored by using a UAV (Falcon 8 octocopter by Astec Ascending Technologies, Fig. 4) with a mounted and calibrated Sony camera Nex 5 (internal orientation is known and was used for the processing, focal length 16.409 mm, resolution 14 Megapixel). The system comes with a remote control and an autopilot system (altimeter, GPS, inclination sensors, gravity sensor) and can be operated both manually by the remote control and automatically using an external PC and a flight plan. Due to the very complex topography of the slope and very windy conditions during the flights, the UAV was operated manually by the pilot in both cases without using a flight plan and with variable flight heights between 50 and 80 m overground. Table 2 shows the important values for the two flight campaigns. During the flights, a sum of 48 to 158 pictures with an overlap of at least 60 % were taken. For the production of orthophotos and 3-D point clouds of the area, an exterior orientation was necessary (Lindner, 2009). Thus a sum of 31 to 37 true ground points (red crosses in the case of the 2013 campaign and red carpets with a reflector in the center for the 2015 campaign) were distributed over the slope (Fig. 4) and measured in the field by using a differential GNSS antenna. In order to adjust all ground control points (GCPs) in one common and stable global coordinate system (UTM 32N ETRS 89 with ellipsoidal heights/EPSG:25832), during the 2015 campaign one fix point was measured with a Stonex S9III GNSS antenna by using RTK information (RTK Fix by NTRIP) from an Italian service (Topcon positioning/GeoNRTK by Geotop Italia – www.geotop.it). Due to the unstable availability of the mobile network, this fixed point was used as base position for a rover-base system (Leica GS09 differential GNSS antenna with radio transmission of an own correction solution). Using this system in combination with a Total Station (Leica TPS 1205), all GCPs and the TLS reflectors (see Fig. 3) of the 2015 campaign were measured with a 3-D accuracy below 3 cm. As the RTK information was only available during the 2015 campaign, the 2013 GCPs were adjusted to the 2015 coordinate system by using the 2015 coordinates of TLS reflectors as control points and Leica GeoOffice to shift them (module shift). The comparison of the coordinates of the two campaigns shows a mean deviation below 0.05 m (for details see Table 2).

In order to produce ortho-images and photogrammetrically derived point clouds, the raw data (photographs and GCP) were processed by using the software PhotoScan Pro (Agisoft/version 1.1.6; see Fig. 5). We used both the information of the camera calibration and an external orientation.

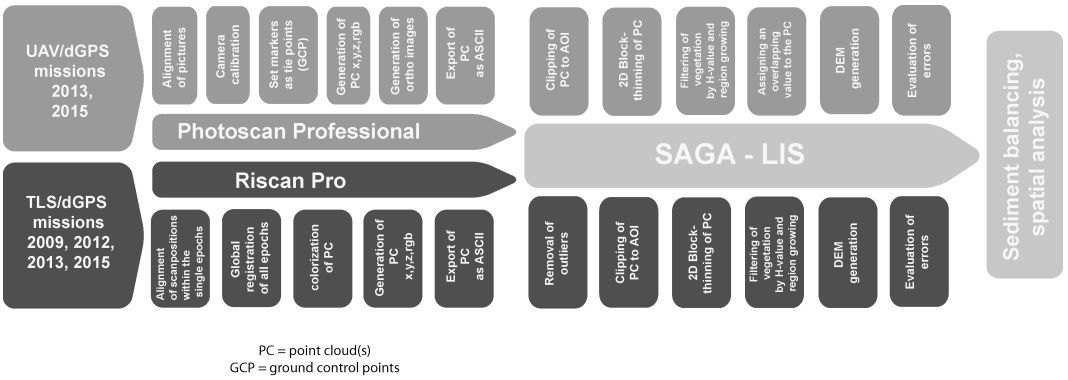

Figure 5. Workflow of the processing steps in PhotoScan Pro, RiscanPro, and LIS/SAGA GIS.

For the internal orientation we used the data from our camera calibration and the camera calibration tool of PhotoScan Pro. The external orientation was conducted by a manual adjustment of the measured GCPs. The accuracy of the exterior orientation (by GCP) of the single campaigns shows a mean deviation of 0.034 to 0.048 m (Table 2).

The resulting dense point clouds were ASCII-formatted (x, y, z, and RGB values) and exported in order to use LIS Desktop/SAGA GIS for the subsequent processing steps (Sect. 3.2). The referenced orthophotographs (UTM 32N ETRS 89 EPSG:25832) were exported as referenced TIF files with a ground resolution of 0.05 m for all epochs. These pictures were used afterwards for visualization and for a visual interpretation/validation of the results.

3.2 Processing of the raw point clouds, DEM derivation, and spatial analysis

After the global co-registration in RiscanPro and PhotoScan Pro, TLS and SfM point clouds were both imported into the LIS / SAGA GIS environment (LIS desktop and LIS workstation) for the further steps of processing and analysis.

These steps can be separated in point cloud thinning, vegetation filtering, filtering by the value overlapping (only UAV SfM data), a final filtering step, DEM generation, and estimation of errors.

3.2.1 Point cloud thinning

Positive and negative outlier points (e.g., flies, birds, or dust) were automatically removed by a filter based on the elevation variability (dZ: 1.5, number of neighbors: 15) of points in a specified point neighborhood. This was only necessary for the TLS data set, as SfM data did not show such outliers.

The areas of interest (AoIs) were manually mapped as polygon shape files, in order to exclude dense vegetation (tree and shrub areas) and to reduce the processing time for the subsequent processing steps (see Fig. 2); thereby the AoIs of the UAV SfM and TLS data were slightly different. As the windy conditions during the 2015 UAV campaign did not allow a satisfactory image overlap in the upper slope parts, we decided to analyze UAV data on the basis of a smaller AoI than the TLS data. The comparison of the results of both methods was done on the basis of the smaller UAV AoI.

Two-dimensional block filtering was applied in order to reduce redundant points on surfaces close to the scanner (filtering method: nearest, horizontal spacing: 0.4 m). This step led to a reduction of the overall number of points and to a reduction of the maximum point densities.

3.2.2 Vegetation filtering

To eliminate hindering vegetation, a two-step procedure, consisting of color-based and structure-based filtering, was carried out.

The RGB values provided by the SLR camera of the scanner or the photogrammetric data for each measurement point were converted to the HSV color space (Haas et al., 2011), which allowed for a deletion of all green hued points (as supposed by us to represent vegetation). This color-based filter approach was not successful in removing all vegetation points, as quite some vegetation on the mine slope is either gray or light red colored (especially dead vegetation).

Therefore a region growing algorithm preceded by a parameter-controlled segmentation algorithm and a rule-based classifier were subsequently applied to split the data set into ground and non-ground points (c.f. Ying Yang and Förstner, 2010; Bremer et al., 2013).

3.2.3 Image overlap of the UAV SfM point cloud

The overlapping values (as sum values for the single zones) were calculated by a reclassification of the colorized (RGB values) overlapping map, that was exported as a TIF file from the PhotoScan Pro report and where the UAV (camera) positions are marked (only available as a pdf file). The TIF file was referenced on the basis of the UAV coordinates, also given by the software and which were exported as x, y coordinates using ESRI ArcMap. The GeoTIFF produced was then imported to SAGA GIS where the RGB values (the

value for overlapping) were assigned as additional attributes to the filtered point cloud. Using the RGB information, the H values (hue value of the HSV color model) for every single point of the point cloud were derived and also added to the filtered point cloud. By a reclassification of the H values, the number of overlapping pictures could be added to every single point of the point cloud. Based on this value, the AoI of the UAV data was derived for points with an overlap of at least eight images.

3.2.4 Final filtering step

In order to produce consistent data sets, a raster data set of all single epochs (UAV and TLS) was produced, which provides the information of vegetation (as a no-data value) or true ground (value 1). All subsequent steps of analysis are based on this consistent filtering result.

3.2.5 DEM generation and spatial analysis

The resulting ground points were aggregated to a DEM with $0.2\,\mathrm{m} \times 0.2\,\mathrm{m}$ cell size, which proved to be the best compromise between the best possible resolution and the lowest number of cells without a representing point in the point cloud (no-data cells). Gridding was achieved by using a moving plane approach. A best fit plane was calculated from the z values of the 12 nearest neighbor points within a 0.1 m search radius to the cell center. Starting with the point cloud, a grid is placed over all the points. Next, for each grid cell center, the 12 points closest to the cell centers in 2-D space are chosen. Where no 12 points are located in a grid cell, the algorithm is allowed to search for points up to a distance of 1.5 the grid cell length from the cell center. Now, least-squares 2-D regression minimizing vertical distances to the plane (as opposed to orthogonal distances) is applied to fit a plane that represents the selected points within the cell. Finally, the z value on the regression plane at the xy location of the grid cell center is used as the DEM cell value.

As the gridding method of moving planes can result in artifacts next to no-data areas, the no-data areas were enlarged by two lines of cells after the gridding procedure to remove these artefacts was carried out.

The spatial analysis was done with terrain analysis tools of SAGA GIS 2.2.0. In order to analyze the geomorphic changes on the slope during the 5 1/2 year time period, we used the stream power index (Moore et al., 1991) for three single epochs (2009, 2013, and 2015; 2012 was excluded as surface changes were low during this periods) as proxy for the exposure to fluvial erosion:

$$\mathrm{SPI} = \mathrm{SCA}\tan(\mathrm{slope}), \tag{1}$$

where SPI is the stream power index, SCA is the specific sediment contributing area (Quinn et al., 1991), and the slope was derived after Zevenbergen and Thorne (1987). The changes of the SPIs of all single time steps and for the whole period were used to visualize and analyze the changed erosion potential over time.

3.2.6 Error assessment

To estimate the error of the TLS and the photogrammetric data, Gaussian error propagation was applied as described in detail within the next section.

3.3 Sediment balancing

As all point clouds contain measurement errors that need to be accounted for, these errors are propagated into the resulting DEMs. For a quantification of the error in DEM values, we adapt a statistical approach and assume that the errors of the grid cells follow a normal distribution with a mean of zero and that the overall DEM error can be expressed by a standard deviation (Taylor, 1997; Burrough and MacDonnell, 1998).

The absolute value of each grid cell in the DEM of difference (DoD) is then related to δ_{DoD} to calculate a t score, and a simple t test is conducted for each cell to arrive at a decision as to whether the change is significant or not.

$$t = \frac{|Z_{\mathrm{DEM2}} - Z_{\mathrm{DEM1}}|}{\delta_{\mathrm{DoD}}} \tag{2}$$

We apply a simple probabilistic threshold at the 95 % confidence interval to classify DoD cells as probably representing real change or measurement error. Only the cells classified as displaying real change are used for budget calculation. The spatially uniform height difference error δ_{DoD} can be used to arrive at an estimate of the total volumetric error of all n raster cells with cell size c in the DoD (Lane et al., 2003).

$$\delta_{\mathrm{DoD}}\sqrt{nc^2} \tag{3}$$

The errors of the individual DEMs are usually estimated via a comparison of the two different measurements between which the observed surface has not changed, or by use of a stable area approach (Westaway et al., 2000). As repeat measurements would have been too time-consuming for both TLS and UAV for this study, the stable area approach was used for error assessment. These areas are distributed over the whole slope (Fig. 10a) and we carefully chose areas of which we knew that no surface changes occur on these areas during the single epochs. The standard deviation of the DoD cells in these areas represents the value δ_{DoD} from Eq. (2).

Based on these errors, the resulting δ_{DoDs} were then applied within the budgeting process of each TLS and UAV epoch combination; the single values can be found in Table 3.

3.4 Comparison of TLS and UAV data

As data from two different methods were available for the detection of surface changes in the study area, both the single data sets and the results of the sediment balancing were compared. This comparison was done in two steps.

Table 3. Standard deviation and LoD (at a 95 % confidence interval) in meters for the single TLS and UAV epochs derived on the basis of the stable areas.

Epoch	2009–2012		2012–2013		2013–2014		2014–2015		2009–2015		2013–2015	
Method	TLS										UAV TLS	
	σ	LoD	σ	LoD	σ	LoD	σ	LoD	σ	LoD	σ	LoD
	0.035	0.097	0.013	0.036	0.036	0.100	0.015	0.042	0.024	0.067 0.035	0.039 0.097	0.108

UAV DEM to TLS DEM comparison and comparison of point densities of UAV and TLS data was carried out as follows.

- Point densities for UAV and TLS data were derived as the raster data set with a resolution of 1 m (this forms a standardized value for the presentation of point densities) on the basis of the filtered point clouds.
- Using the 2013 filtered data, the UAV-DEMs and the TLS-DEMs were compared based on the smaller AoI of the UAV data. Therefore a DoD of both data sets was produced by not including a level of detection (LoD). Afterwards a qualitative as well as a quantitative analysis was conducted.

Comparison of the sediment balancing was also carried out as follows.

- The results of the sediment balancing of the TLS and the UAV data for the equal epoch (2013 to 2015) were compared. The result was also used for quantitative and qualitative analysis.

4 Results and discussion

4.1 Comparison of TLS and UAV data

Different point density, different point distribution, and the differences in the LoDs as well as inaccuracies of the registration procedures may have effects on the results of the calculated volume balancing presented in Sect. 4.2. Thus, for the understanding of these results it seems necessary to compare both used methods in detail. In order to prepare the quantification and analysis of surface changes by UAV and TLS, this section provides a thorough analysis of a comparison of both data sets in the means of resolution (point density) and fitting (UAV-DEM to TLS-DEM). The detailed results of the quantification of surface changes will be compared, following Sect. 4.2.

4.1.1 Comparison of the resolution

The comparison of the point densities of the filtered point clouds of the 2013 UAV and TLS data (the 2015 data provide similar results) shows considerable differences (Fig. 6). While the maximum values of the TLS data are much higher (but with a large scattering, Table 1), the UAV data are much more homogeneous with a low scattering.

TLS data

- The high densities of the TLS data can be found at overlapping areas (overlapping of scans of one or more scan positions) and at the regions close to the scan positions, which is the consequence of the adjustable angle resolution. During the scanning campaigns, an angle resolution of 0.05° was used. Thus the distances between the measured points are smaller at regions close to the scanner and vice versa.
- Low densities of the TLS data are distributed over the slope and are the consequence of shadowing effects, vegetation cover, unfavorable incidence angles of the laser signal (especially in flat areas), and areas with fewer scan positions.

UAV data

- The UAV data show a lower maximum of the point density, but the distribution is very homogeneous. Thus the mean point densities are higher than all the TLS point densities of the single epochs (Table 1).
- The mean values of the 2013 and 2015 data are identical although the data are based on a very different number of pictures (Table 1).
- Point density is also constant in areas with a complex surface topography, which is the consequence of the bird's-eye view with shadowing effects only beneath lower vegetation.
- Following the filtering process, areas with vegetation cover provide only low point densities. As the UAV records the AoI from the bird's-eye view, only few ground points remain after the filtering procedure. This effect is the stronger the denser and lower the vegetation is, especially for shrubs that can be found in the sparse vegetation areas. Thus no surface information can be provided for these areas by the UAV data.

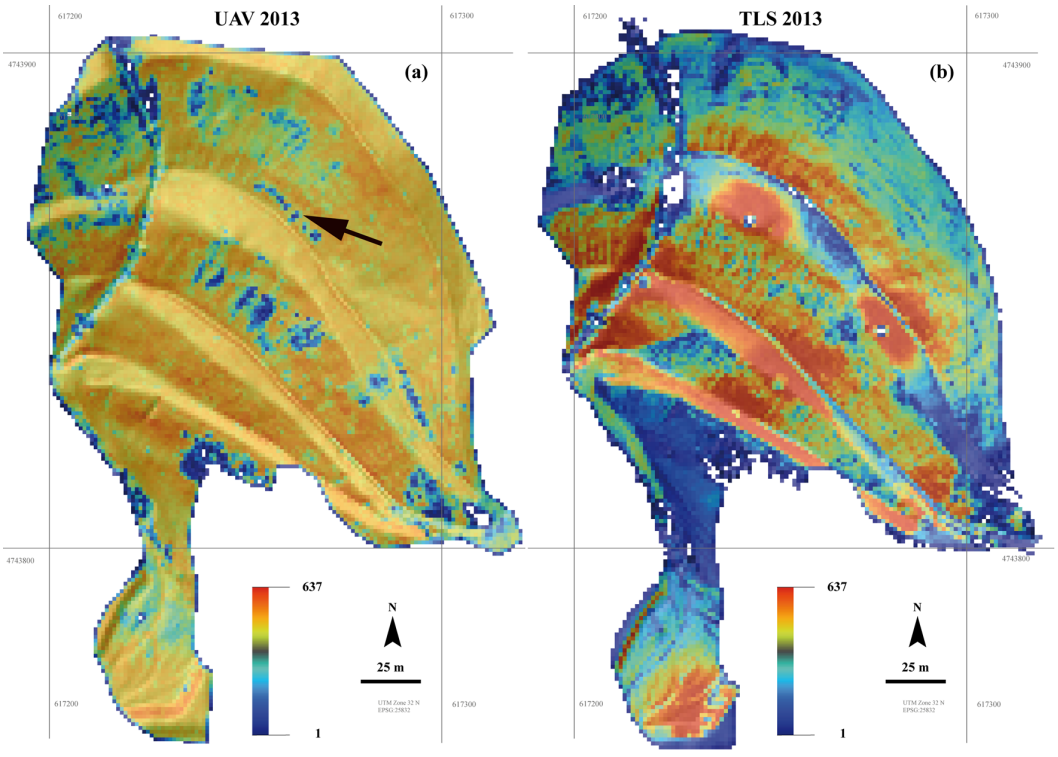

Figure 6. Comparison of the point density (points per m^2) for **(a)** the 2013 UAV data and **(b)** the 2013 TLS data.

– Low point densities can also be found in areas with a very homogeneous surface structure (light colored and very smooth surface, arrow in Fig. 6). Obviously the SfM algorithm has problems detecting similar points in both the 2013 and the 2015 pictures.

4.1.2 Comparison of UAV and TLS DEMs

An exemplary comparison of the UAV-DEM and TLS-DEM was conducted by producing a DoD of both data sets (Zdiff) on the basis of the filtered data of the 2013 campaign (2015 data provide similar results). Figure 7a shows no systematic errors between both data sets. The mean value lies close to zero (0.006 m), with a standard deviation of 0.049 m (for the values see Fig. 7b). These results are comparable to the values presented by Prosdocimi et al. (2015), which compared terrestrial SfM and TLS in a study on channel bank erosion in an agricultural landscape in Italy. The results of the presented work indicate a very good fitting of both data sets and a very stable global registration of the TLS data. It can therefore be stated that the global registration of the UAV data by using RTK GNSS, and of the TLS data by only using tie points on the wooden construction on the left part of the AoI, in combination with the ICP algorithm in RiscanPro (cf. Sect. 3.1.1), seems successful. Nevertheless there are areas which show higher differences between UAV and TLS DEMs than others. Comparing Figs. 6 and 7a indicates that the highest differences appear predominantly in areas with low point densities, which are the consequence of the different acquisition methods discussed above (especially the viewing angles). This qualitative analysis can be supported by a statistical observation, which is presented in Fig. 7b. Therefore the point density values of the inhomogeneous TLS data were separated into five classes (< 5, 5–10, 10–15, 15–20, > 20) and afterwards compared with the DoD of the UAV-DEM and the TLS-DEM. It is clearly visible that with increasing point density, the standard deviation becomes lower as well as the mean value getting closer to zero. Thus it can be stated that point density and especially an inhomogeneous distribution of point densities, as is the case for the TLS data in this study, must be seen as an important influencing factor for the detection as well as for the quantification of surface changes. Consequently, these results will be taken into account for the discussion of the subsequent quantification and analysis steps.

4.2 Quantification of surface changes

4.2.1 Quantification of surface changes by TLS data

The TLS repeat measurements yielded a LoD between 0.036 and 0.100 m (Table 3) for the single epochs. Thus the volumetric surface changes in Table 4 comprise only surface changes over the respective LoDs. The overall balance for the 2009 to 2015 epoch was not derived by summing up the values of the single epochs but by using only the 2009 and

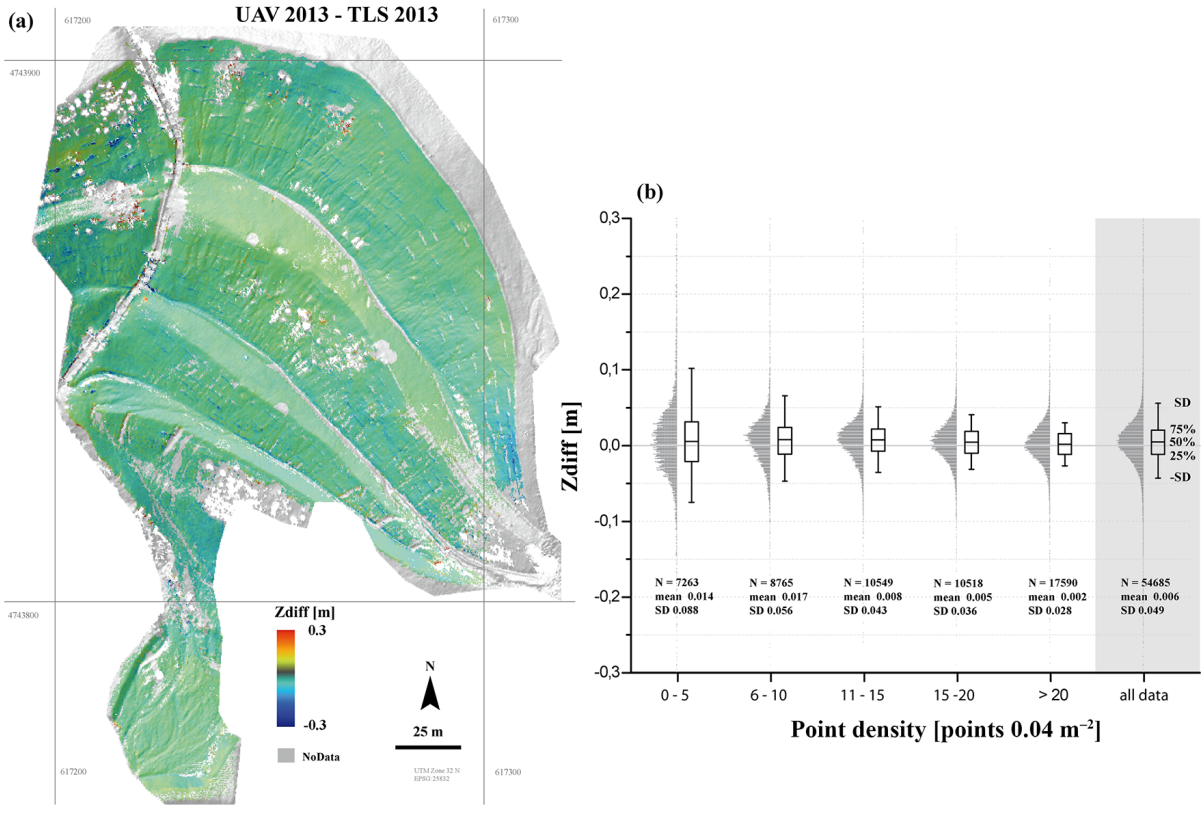

Figure 7. **(a)** Comparison of the 2013 UAV and 2013 TLS DEMs (not using the LoD) and **(b)** the distribution of Zdiff (UAV 2013 and TLS 2013; mean value of Zdiff for the whole data is 0.004 m) and the dependence of Zdiff from the point density (point density is divided into five classes and presented for the whole data set).

Table 4. Sediment balancing (only values over the LoD) for the area of interest (AoI) and separated for the slopes and the reservoir for all epochs of the TLS measurements.

	AoI			Slope	Reservoir
Epoch	Cut	Fill	Balance	Balance	Balance
2009–2012	$-75.41\,m^3$	$30.78\,m^3$	$-44.62\,m^3$	$-65.82\,m^3$	$20.58\,m^3$
2012–2013	$-32.37\,m^3$	$59.76\,m^3$	$27.39\,m^3$	$32.37\,m^3$	$-2.65\,m^3$
2013–2014	$-47.28\,m^3$	$90.80\,m^3$	$43.52\,m^3$	$-23.3\,m^3$	$64.58\,m^3$
2014–2015	$-55.71\,m^3$	$127.90\,m^3$	$72.19\,m^3$	$35.50\,m^3$	$36.39\,m^3$
2009–2015	$-188.28\,m^3$	$191.54\,m^3$	$3.26\,m^3$	$-134.61\,m^3$	$137.96\,m^3$
2013–2015	$-82.15\,m^3$	$176.33\,m^3$	$94.18\,m^3$	$-21.70\,m^3$	$118.45\,m^3$

2015 DEMs. As between the single epochs, surface changes may vary from erosion to accumulation; the sum of the single epochs and the comparison of the 2009 to 2015 epoch differ clearly.

As there are detectable volumetric changes of $-188.28\,m^3$ (erosion) and $+191.54\,m^3$ (accumulation) for the epoch 2009 to 2015, the sediment balance seems to be even or slightly positive. As expected, most of the erosion takes place on the slope and the accumulation is concentrated in the reservoir (Fig. 8).

Erosion on the slopes can be separated into areas with sheet erosion and areas that show rill erosion or erosion in channels and sums up to a value of $-134.61\,m^3$. The pattern of erosion is comprehensible from a geomorphic point of view, but shows a few inconsistencies, which are exemplarily highlighted in Fig. 8b to e. Figure 8b and d show two examples (more of them are visible all over the AoI) for the missing information due to shadowing effects in areas with a complex topography, which is the case in and around the constructed channel and in the incised gullies and channels (and

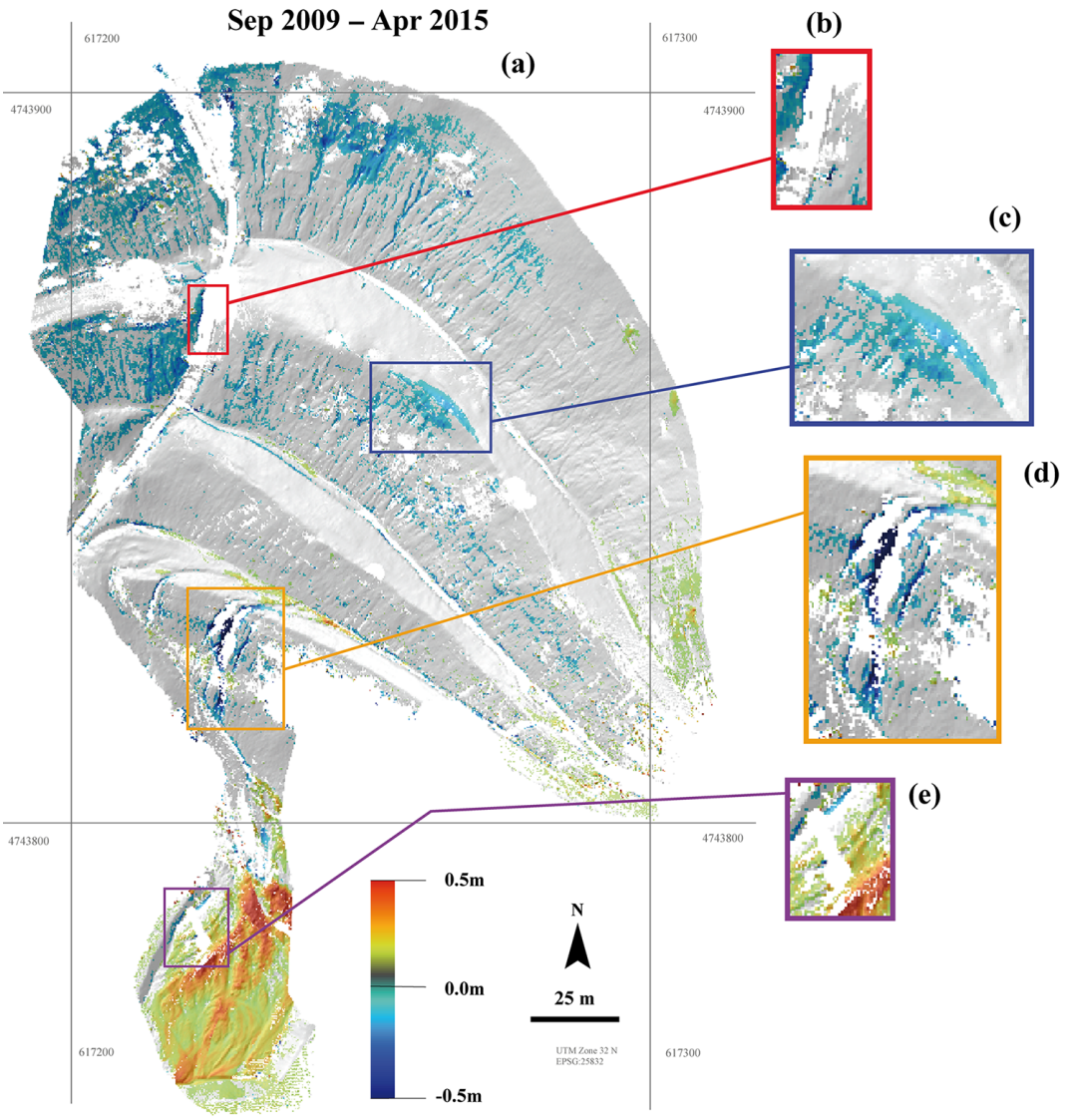

Figure 8. Surface changes (over the LoD) on the AoI for the 2009 to 2015 epoch of the TLS measurements.

of course in the areas with vegetation, which are not highlighted). This missing information, especially in the gully, certainly leads to an underestimation of the erosion on the slopes. Beside this, Fig. 8c shows sheet erosion on the top of the slope with the lack of a downslope connection. These surface changes are in fact not the result of erosion by water but the consequence of subsidence in this area, which could be verified in the field. Thus this surface change should strictly not be applied to the volumetric changes by fluvial erosion (in fact it was excluded from the volumetric balancing).

Most of the accumulation in the AoI is concentrated on the flat surfaces as e.g., on the terrace over the gully in Fig. 8d and on a slope in the eastern part of the AoI. The accumulation on the terrace is the consequence of a shifting of the channel during a high precipitation event on this terrace and a displacement of the gully system from west to east (for detail see Sect. 4.2.2). The accumulated material is delivered from the small channel on the bottom of the slope and a small upstream gully, which is not detectable by the TLS data but by the UAV data (see Sect. 4.2.2). The accumulation on the western slope is also caused by a heavy rainfall event, where water and material was transported over the terrace (which is outside the AoI) onto the slope. Traces of this overflow could be verified in the field.

However, most of the accumulation within the AoI took place on the surface of the reservoir. The pattern of accumulation is also comprehensible from a geomorphic point of view and is the consequence of high discharge events between 2009 and 2015 (Fig. 11). Taking only the 2009 to 2015 epoch into account, the surface changes in the reservoir are predominantly positive and show only accumulation, which indicates that the reservoir acts as a sediment sink. Both the

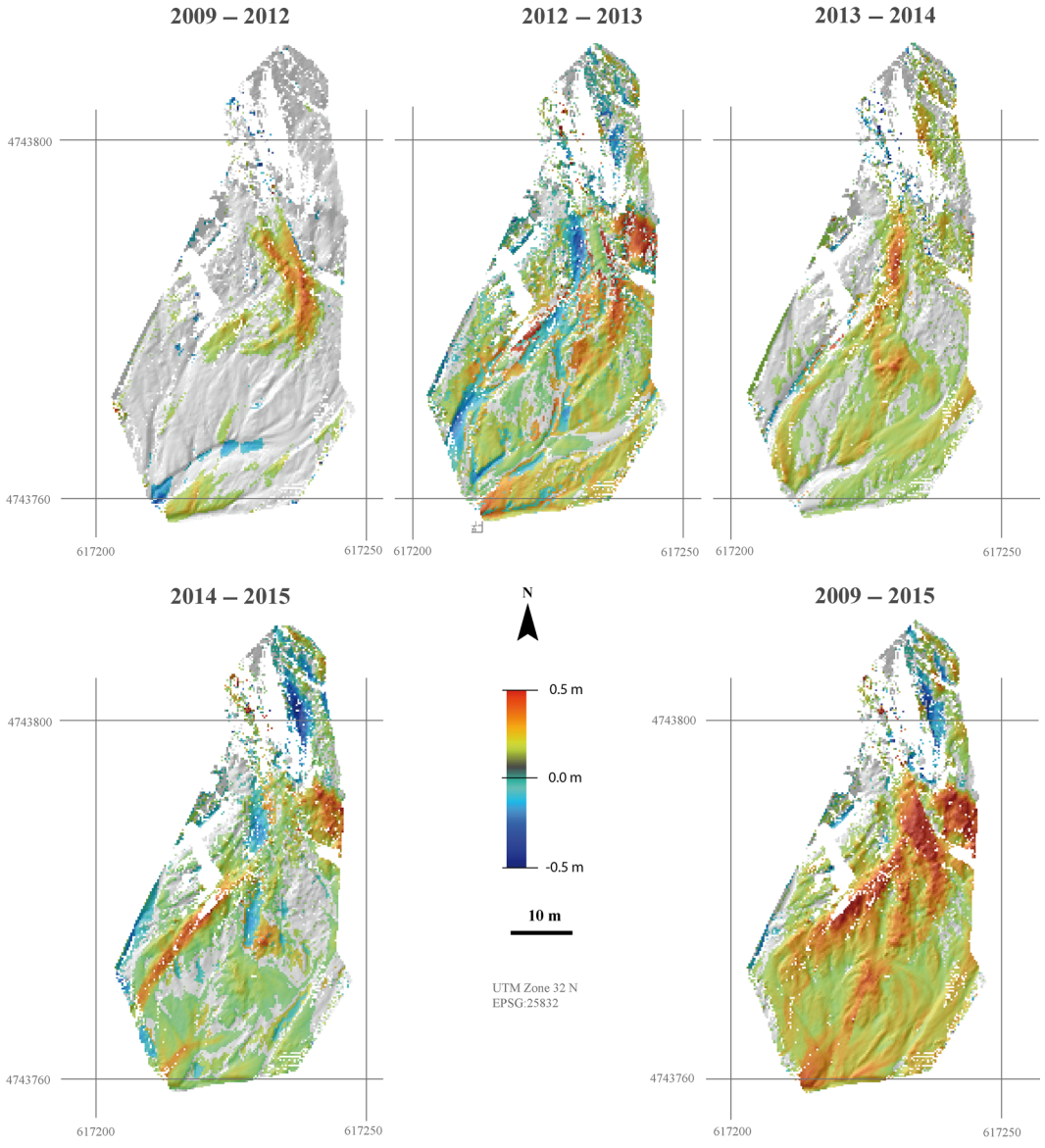

Figure 9. Surface changes (over the LoD) in the reservoir for the single epochs between 2009 and 2015 derived on the basis of the TLS data.

sediment balancing in Table 4 and the surface changes in Fig. 9 for all single epochs show that there is not only accumulation but also erosion present in the reservoir. Thus it seems that sediment leaves the AoI during events with higher runoff. As on the slopes, there are also areas affected by shadowing effects. One of these is highlighted in Fig. 8e and shows an area with no data under and behind a shrub (see also Fig. 4b). These no-data areas can also lead to an underestimation of the volume balancing.

Summing up the discussed results of the TLS data, the positive sediment balance seems to be unrealistic, especially in the context of erosion, and probable through transport of material onto the surface of the reservoir. This fact indicates the transport of material out of the AoI, and thus the sediment balancing had to be expected as clearly negative. The reasons for the even or slightly positive sediment balance are as follows.

– There is a clear underestimation of erosion on the slopes because of (i) no data values beneath vegetation on the eastern part of the slope and (ii) because of shadowing effects due to a very complex surface topography. Especially the complex gully structure in Fig. 8d leads to a loss of information in an area with heavy erosion. Beside this (iii) the level of detection varied between the single epochs and the 2009 to 2015 epoch. Slight erosion processes (e.g., erosion by sheet flow) are only detectable if they have a magnitude over the LoD. While

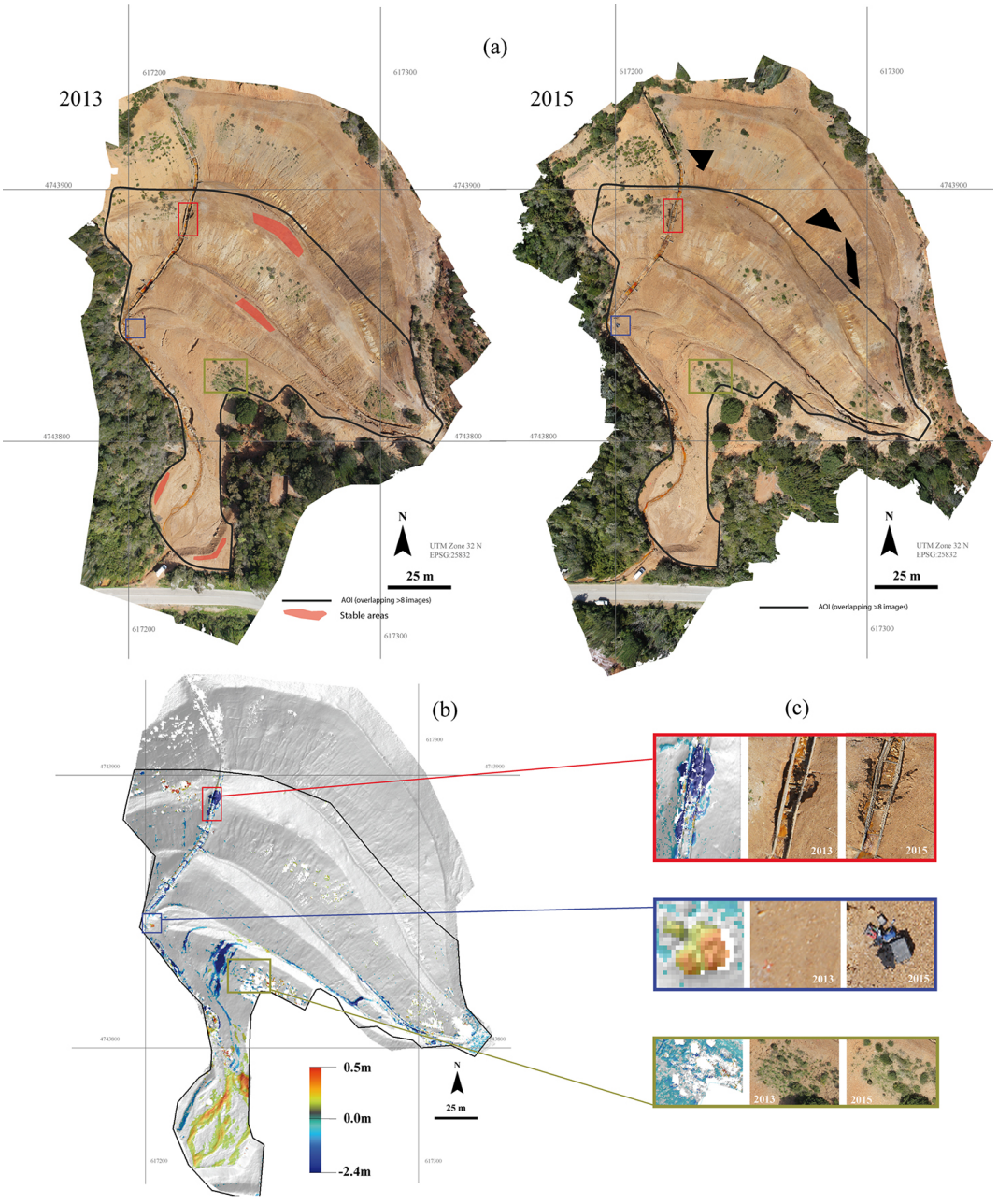

Figure 10. **(a)** Aerial photographs of the 2013 and 2015 UAV epochs with the AoI and the stable areas used for error estimation, **(b)** the surface changes for the period 2013–2015 for the AoI, and **(c)** enlargements of special areas/features.

the surface changes in the reservoir are limited on the narrow reservoir, which leads to surface changes over the LoD, it can therefore be assumed, that especially erosion by sheet flow on the slope is underestimated in the sediment balancing.

– The accumulation in the reservoir seems to be well represented, but Table 4 and Fig. 9 show that there are also uncertainties due to the alternation of erosion and accumulation. This probably leads to an overestimation of the accumulated material for the 2009–2015 epoch in contrast to the sum of the single epochs.

– An important factor in comparing sediment sources and sediment sinks is the different bulk density of source material and accumulated material. As source material normally has a higher bulk density, fluvial accumulated material normally is less dense, which probably leads to a difference in the calculated volumes based on measured surface changes.

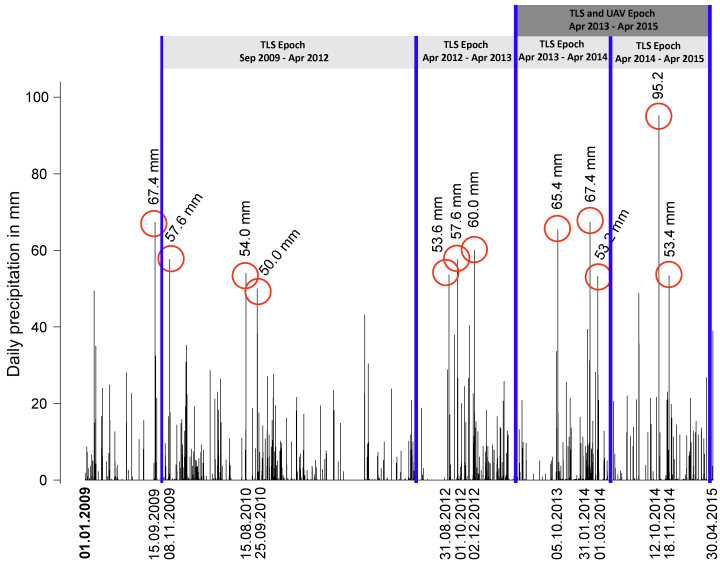

Figure 11. Daily precipitation at the Vecchia Aurelia metro station in the northeast of Piombino (UTM coordinates: 631512.00 E, 4764190.00 N) for the period April 2009–April 2015, provided by the Servizio Idrologico Regionale (www.sir.toscana.it).

– A few of the described problems are the consequence of the unfavorable viewing angle of TLS, especially on surfaces with a complex topography. To investigate if a bird's-eye view can minimize the effects of shadowed areas, volume balancing by UAV-based SfM was conducted.

4.2.2 Quantification of surface changes by UAV data

Similar to the TLS data, the UAV data also show a consistent pattern of surface changes within the AoI for the 2013 to 2015 epoch (Fig. 10). The highlighted areas in Fig. 10c show that surface changes are very well detectable even within the very complex surface topography around the constructed channel (Fig. 10c red) and that vegetation is quite well filtered by the filtering workflow used (Fig. 10c green). Figure 10c (blue) shows an artificial surface change due to the presence (2015) and absence (2013) of the UAV transport box and backpacks of the investigators. This can be used for the evaluation of the accuracy of the measured surface changes, as the volume of the transport box is well known. The measured artificial surface changes by the DoD fit quite well to the known box dimensions (difference of $\sim 10\,\%$).

The surface changes on the AoI can be separated into three major parts. (i) Fluvial rill erosion by concentrated flow on the steep slopes is only slight with no visible accumulation on the corresponding flat areas between the slopes. (ii) Surface changes on the eastern part of the middle slope and on the whole lower slope are indicating intensive gullying by concentrated flow. These gullies belong to one channel system that has its origin on the topmost terrace outside of the AoI (Fig. 2a). As a consequence of the increasing catchment size and due to the shifting of the channel system already described, the "gully complex" on the lower slope consists of three single gullies, with the highest surface changes on the eastern gully (deepening of up to 2.4 m). These very high erosion rates can be seen to be a consequence of very heavy rainfall events between April 2013 and April 2015. Precipitation data of the Vecchia Aurelia metro station (Fig. 11) show three rainfall events higher than $50\,\mathrm{mm\,day^{-1}}$ for this region in winter 2013/2014 and two in autumn/winter 2014/2015, with the highest one in October 2014 ($95.2\,\mathrm{mm\,day^{-1}}$). (iii) The flat embanked area (sediment reservoir) on the bottom of the slopes shows both zones of accumulation and erosion. While the central part is dominated by accumulated material, the western part shows linear erosion, starting at the eastern gully of the described lower slope. The pattern of accumulation as well as erosion is clearly visible on the DoD and on the aerial photographs and shows a braided river system, including lateral erosion on the western dam. This fact indicates transport of material out of the AoI. This through transport of material at the sediment reservoir and the good resolution of the erosion within the gullies explain the clearly negative sediment budget of $-43.21\,\mathrm{m^3}$ (Table 5); but this value must be seen as a minimum value, as the AoI does not include the upper slopes of the mine.

Table 5. Volume balance based on the UAV and the TLS data for the whole AoI.

Method	Epoch	Cut	Fill	Balance
UAV	2013–2015	$-123.86\,\mathrm{m^3}$	$80.65\,\mathrm{m^3}$	$-43.21\,\mathrm{m^3}$
TLS	2013–2015	$-82.15\,\mathrm{m^3}$	$176.33\,\mathrm{m^3}$	$94.18\,\mathrm{m^3}$

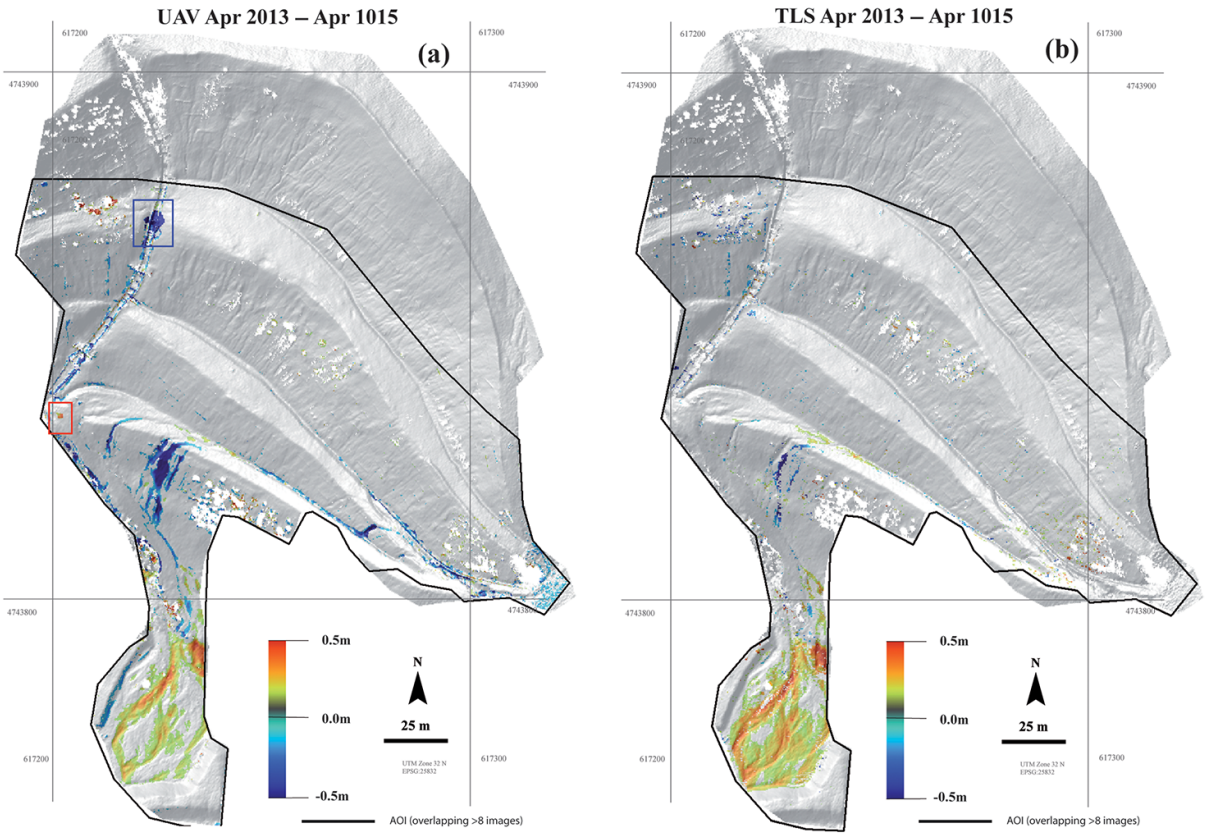

Figure 12. Comparison of the surface changes of the 2013 to 2015 epoch for **(a)** the UAV data (for an explanation of the two squared areas see Fig. 8) and **(b)** the TLS data.

Summing up the discussed results of the UAV data, the negative sediment balance seems to be realistic, but while the heavy erosion in the gullies is well detected, the erosion on the slopes is probably underestimated. Especially in the context of the high LoD of 0.108 m, erosion on the slopes by sheet flow or the erosion in small rills must be seen as not detectable by this special investigation design, as from a geomorphic point of view, such erosion should have taken place on the slopes but is not expected to exceed the value of the LoD (> 0.108 m) during the 2-year survey.

4.2.3 Comparison of the sediment balancing of UAV and TLS data

As mentioned in the preceding sections, the result of the volume balancing of the TLS and the UAV data varied strongly. The first line of table 5 shows that while the TLS-based volume balancing results in a positive balance, the balance of the UAV data is clearly negative. These differences are the consequence of both an underestimation of the erosion on the slopes by the TLS data and an underestimation of the accumulation in the reservoir by the UAV data. Both effects are also clearly visible in Fig. 12.

- Due to the above-mentioned shadowing effects, the erosion within the incised gullies or around the constructed channel is not detectable by TLS with the investigation design used (location of the scan positions). Due to the bird's-eye view of the UAV, surface changes in the complex areas are very well detected and do not show data holes within those regions.
- Surface changes within the reservoir are much better detected by the TLS data (except the undercutting of the eastern dam). While the pattern of the accumulation area is very similar between UAV and TLS data, there are also very low surface changes identified in the TLS data, which show no surface changes in the UAV data. This is probably the consequence of the higher LoD of the UAV data (Table 3), as only surface changes over 0.108 m are identified as significant surface changes.

As the visual comparison of the TLS and UAV data in Fig. 12 only shows the differences between the no-data values and the measured surface changes, Fig. 13 provides information about the comparison of the surface changes that are detected as surface changes in both data sets. Taking the results in Sect. 4.1 and the results in Fig. 12 and 13 into account, it seems that there is no systematic error (e.g., because of a

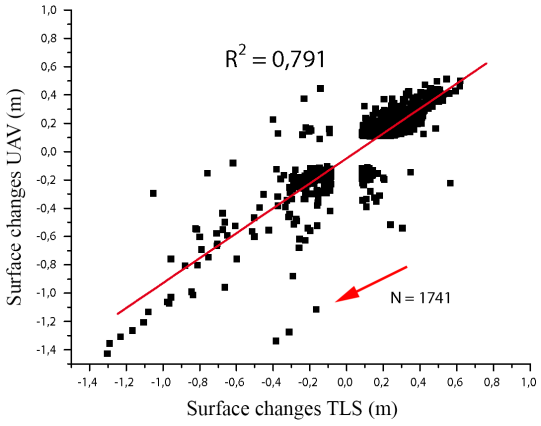

Figure 13. Comparison of surface changes of the 2013 to 2015 epoch for the UAV and the TLS data, which are detected in both data sets.

shifting of one data set) detectable as e.g., James and Robson (2014) described for their UAV data (e.g., bowl effect). Such errors could probably be minimized in this study by distributing the GCPs also close to the borders of the investigated slope, by using the factor overlapping in order to generate a stable geometry, and by using the values of the internal orientation of the camera. The R^2 of the correlation of the TLS and the UAV data shows a value of 0.791 ($p < 0.0001$). Nevertheless the scattering is partly high in an area where the amounts of erosion are much lower in the TLS data (arrow 1 in Fig. 13). These points are located on or close to the border areas of the main gully on the lower slope and are an effect of the gridding of the point clouds to derive the DEMs. While the point densities of the UAV data are very homogeneous in the main gully, there are no TLS point data available inside the gully. Especially in the border areas there are only few TLS data (and in fact no data of the inner slopes of the gully) available for the DEM generation, which leads to higher surface values in contrast to the UAV data. Despite the enlargement of no-data areas during the DEM generation process (Sect. 3.2), this effect could not be completely eliminated.

4.3 Analysis of the geomorphic changes by using the stream power index

Figure 14a shows the changes of the stream power index (SPI), as proxy for the erosion potential, between 2009 and 2015 for the whole slope. It is evident from this that the geomorphic processes (especially fluvial erosion) lead not only to the high amounts of erosion and deposition already discussed, but also to changes in the hydrological conditions. These changes can also be seen in the distribution of the SPI (Fig. 15). While the mean logarithmized SPI values (SPI is log-normal-distributed) show only a slight switch of the SPI from −0.252 to −0.309, the maximum value increased from 3.249 to 3.489. This slight shifting is the consequence of an ongoing back-cutting of the hillslope channels up to the flat terrace (Fig. 14b). This corresponds with an enlargement of their hydrological catchment (increasing values of the SPI at the channel heads) and first indications of a beginning dissection of the terrace (arrows in Fig. 14b). From a prognostic point of view it is to be expected that this dissection will proceed in the future with a subsequent destruction of the terrace and a coupling of the two bordering slopes.

Such a dissection of a terrace and a coupling of two slopes can already be found at the lowest one (Fig. 14c). The flow paths of the channels already shifted from the west to the east with a consequent coupling of slope sections and steepening of the channel slopes, indicated by the increasing SPI. This fits very well to the massive erosion in the gully structures and the enlargement of the hydrological catchments. While the western gully was still present in 2009, the first eastwards shifting (to channel 2 in Fig. 14c) of the flow parts occurred between 2009 and 2013, probably during high-intensity rainfall events (see Fig. 11; 6 rainfall events over 50 mm day^{-1} were recorded during this period). Between 2013 and 2015 the shifting continued to the easternmost channel (channel 3 in Fig. 14c), with the highest erosion amounts between 2014 and 2015 (indicated by the TLS data and the very high rainfall intensities in this period, Fig. 11). Due to the intensive gullying and the back-cutting of this channel, it seems that the channel is now fixed to this position, with a high erosion potential (indicated by the SPI). It can be expected that this will lead to an ongoing dissection of the bordering terrace and to a subsequent deactivation of the western channels (channel 1 and 2 in Fig. 14c) in the future.

5 Conclusions

The presented investigations show that both UAV and TLS data are suitable methods to detect surface changes on steep slopes and that there is a great potential to quantify and analyze geomorphic processes with a high level of detail, as also stated in the work of Tarolli (2014). Due to the high temporal resolution, but especially the high spatial resolution, these methods offer new perspective for the analysis of geomorphic processes. Beside the potential of the methods, limitations were detected, which have to be taken into account for the interpretation of the results and the use of especially multitemporal data for statistical analysis, modeling, and of course for further investigations.

While TLS offers much better accuracies (LoDs), problems with inhomogeneous point densities and data holes in shadowed areas exist. These effects could be minimized by scanning the surface from more than the scan positions used. This would eliminate both shadowing effects and inhomogeneous point densities. However, it is needless to say that capturing the complex surface of the mine would lead to a much longer stay in the field. Using airborne laser scanning could, however, eliminate the problems with data holes or inhomogeneous point densities due to the more favorable viewing

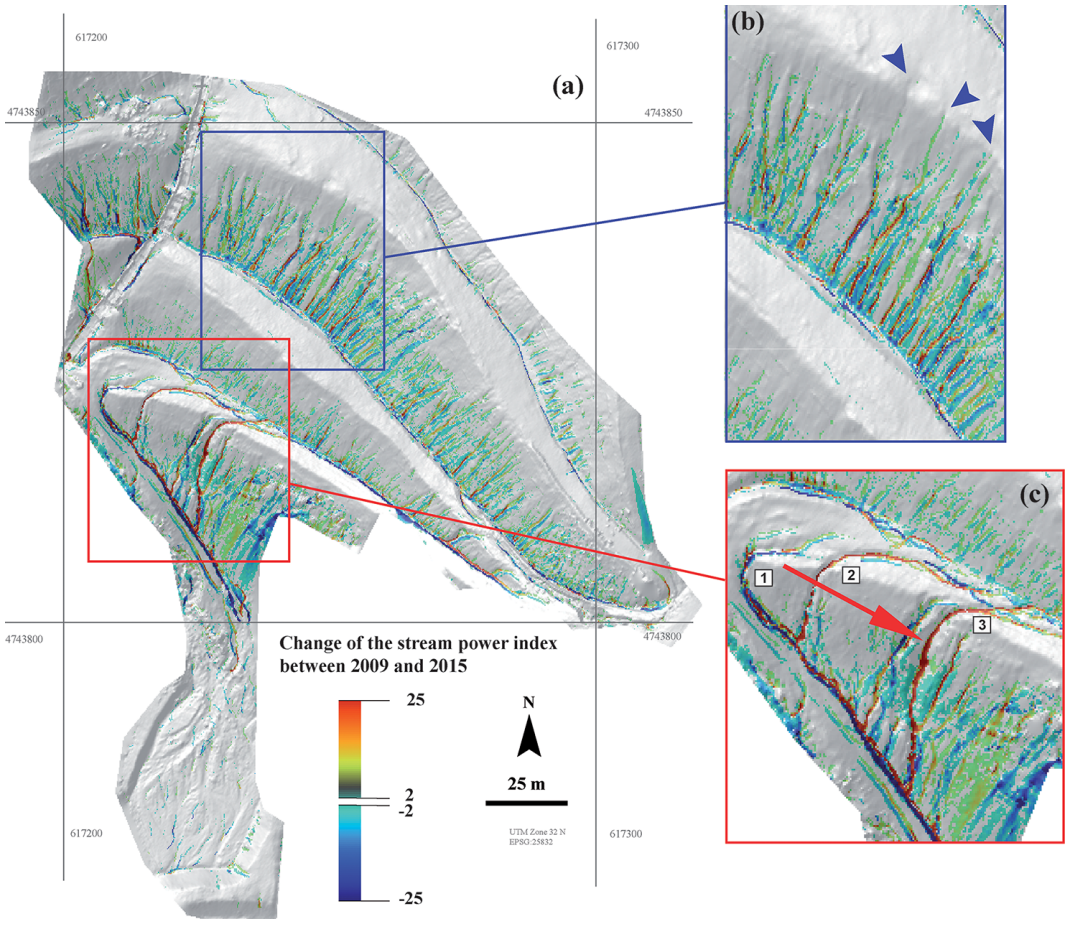

Figure 14. **(a)** Change of the stream power index between 2009 and 2015 for the slope (for better visualization, data from −2 to 2 are excluded), **(b)** back-cutting of channels up to the top of the terrace indicated by the SPI, and **(c)** shifting of the main channel/gully from west to the east with increasing SPI.

angle. As this method needs special aircraft or helicopters, it seems too expensive, especially for such small test sites. However, further developments in the field of UAV-based lidar could also make the method suitable for the monitoring of a very complex terrain.

At the moment it seems that digital photogrammetry by UAV photographs could offer new perspectives for monitoring geomorphic processes in a complex environment with a quick workflow in the field (in this case ∼ 4 h for the slope in contrast to the 2 days for TLS acquisition) and lower costs in contrast to lidar. Due to the bird's-eye view, shadowing effects of e.g., incised gullies do not appear and the intensive gullying is quite well detectable. The disadvantages of the method are the missing data under lower vegetation (e.g., shrub or higher grass), the problems of very homogeneous surface conditions (color, contrast), and the high LoDs in this study. As the high LoD makes it difficult to investigate processes with low magnitudes and processes over shorter time steps (e.g., single events), the LoD should be minimized. This goal could probably be achieved by a lower flight altitude, a camera with higher resolution, or by measuring the GCPs with a more precise total station instead of a differential GNSS antenna in order to reduce the measurement error. All these options normally would lead to a higher resolution of the pictures and a higher accuracy of the global registration, but the expected improvements have to be analyzed during further investigations.

Summing up the study design in this work, both methods show the pattern and the amount of erosion and accumulation of geomorphic processes with magnitudes over the respective LoDs quite well, which can provide important information about the geomorphic process dynamics on such slopes. While processes with high magnitudes (e.g., gullying) are detectable due to high numbers of surface changes even over short monitoring periods, geomorphic processes which cause only slight surface changes are only detectable over longer time intervals. However, as geomorphic processes can overlap in time and space, and the probability increases with time, short monitoring periods are urgently required to distinguish single geomorphic processes (e.g., sheet erosion, rill erosion)

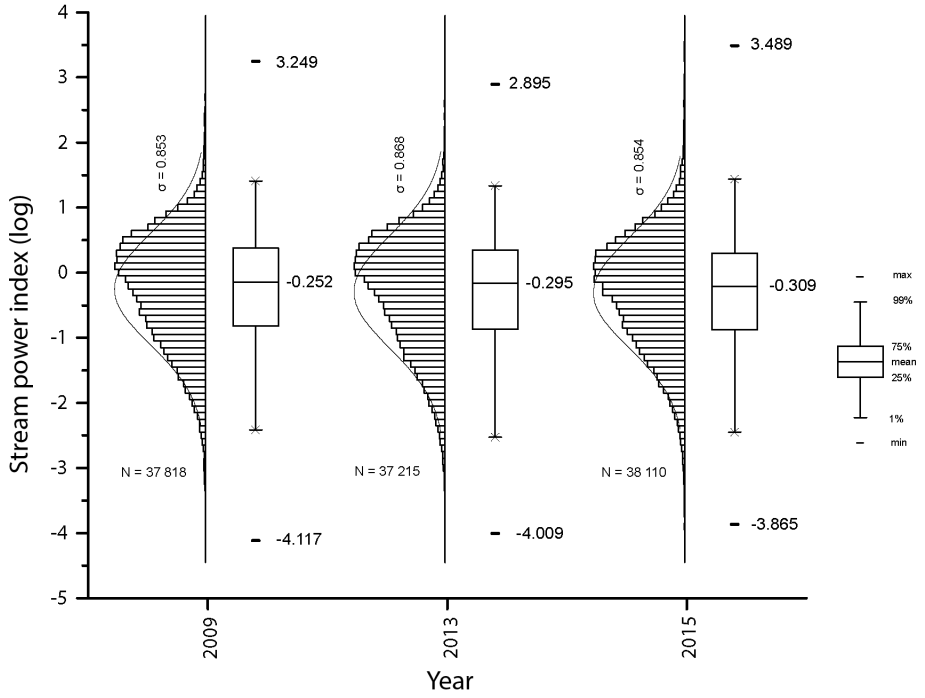

Figure 15. Box plot and statistical distribution of the SPI for the epochs 2009 (TLS), 2013, and 2015 (both UAV).

and, for example, bring them together with e.g., single precipitation events. Therefore future investigations should focus on the opportunities to reduce the LoD of both TLS and UAV data or on the potential and the limitations of a combination of data of both methods.

Beside the methodological aspects, this study showed that the recultivation of the mine must be seen as not sustainable as severe erosion is taking place all over the slope. Most of the artificial structures are now dysfunctional or it has already been 7 years since the recultivation at the beginning of the monitoring in 2009. The predominant geomorphic processes are obviously fluvial processes (beside the singular subsidence), indicated by the intensive gullying and (based on the UAV data) the lateral erosion along the constructed channel. As the analysis of the SPI showed, this fluvial geomorphic activity leads to a massive change of the surface hydrology, with increasing catchment sizes and shortened and steepened flow paths. It is possible that these changes in surface topography will encourage the appearance of bigger mass movements or debris flows in the future.

While reforestation is not feasible due to the very acidic conditions, the artificial slope topography and the artificial structures need an adaption with a subsequent regular inspection and maintenance to control surface runoff, failing which, the slope will become an erosional landscape as it was before the recultivation, including the risk exposure for the adjacent environment (sediments and water contaminated by harmful substances) and infrastructure (e.g., by debris flows or mass movements).

Acknowledgements. As the data were collected during field courses with students for many years, many student generations were involved in their acquisition. They are gratefully acknowledged by the authors. The processing of the data was done within the framework of the DFG (German science foundation) project Questar^{3D} (grant numbers: HA 5740/3-1 and SCHM 1373/8-1). Moreover, the authors want to thank the three anonymous reviewers for their important and useful advice and suggestions during the open discussion process. This valuable input led to an improvement of the manuscript.

Edited by: P. Tarolli
Reviewed by: three anonymous referees

References

Abellán, A., Jaboyedoff, M., Oppikofer, T., and Vilaplana, J. M.: Detection of millimetric deformation using a terrestrial laser scanner: experiment and application to a rockfall event, Nat. Hazards Earth Syst. Sci., 9, 365–372, doi:10.5194/nhess-9-365-2009, 2009.

Aucelli, P. P. C., Conforti, M., Della Seta, M., Del Monte, M., D'uva, L., Rosskopf, C. M., and Vergari, F.: Quantitative assessment of soil erosion rates: results from direct monitoring and digital photogrammetric analysis on the Landola catchment in the Upper Orcia Valley (Tuscany, Italy), Soc. Geol. It., 21, 1199–1201, 2012.

Auerswald, K., Fiener, P., and R. Dikau: Rates of sheet and rill erosion in Germany – A meta-analysis. Geomorphology, 111, 182–193, 2000.

Benvenuti, M., Mascaro, I., Corsini, F., Costagliola, P., Parrini, P., Lattanzi, P., and Tanelli, G.: Environmental problems related to sulfide mining in Tuscany, Chronique de la Recherche Minière, 534, 29–45, 1999.

Bremer, M., Rutzinger, M., and Wichmann, V.: Derivation of tree skeletons and error assessment using LiDAR point cloud data of varying quality, ISPRS J. Photogramm., 80, 39–50, 2013.

Bryan, R. B.: Soil erodibility and processes of water erosion on hillslope, Geomorphology, 32, 385–415, 2000.

Burrough, P. A. and MacDonnell, R. A.: Principles of geographical information systems, Oxford University Press, Oxford, UK, (Spatial information systems), 1st edition, 1998.

Chen, J., Li, K., Chang, K.-J., Sofia, G., and Tarolli, P.: Open-pit mining geomorphic feature characterisation. Int. J. Appl. Earth Obs., 42, 76–86, 2015.

Clarke, M. L. and Rendell, H. M.: Process-form relationships in Southern Italian badlands: erosion rates and implications for landform evolution. Earth Surf. Proc. Land., 31, 15–29, 2006.

Della Seta, M., Del Monte, M., Fredi, P., and Lupia Palmieri, E.: Space–time variability of denudation rates at the catchment and hillslope scales on the Tyrrhenian side of Central Italy, Geomorphology, 107, 161–177, 2009.

Diodato, N. and G. Bellocchi: Assessing and modelling changes in rainfall erosivity at different climate scales, Earth Surf. Proc. Land., 34, 969–980, 2000.

d'Oleire-Oltmanns, S., Marzolff, I., Peter, K., and Ries, J.: Unmanned Aerial Vehicle (UAV) for Monitoring Soil Erosion in Morocco, Remote Sensing, 4, 3390–3416, 2012.

Eltner, A., Baumgart, P., Maas, H.-G., and Faust, D.: Multi-temporal UAV data for automatic measurement of rill and interrill erosion on loess soil, Earth Surf. Proc. Land., 40, 741–755, 2015.

Flener, C., Vaaja, M., Jaakkola, A., Krooks, A., Kaartinen, H., Kukko, A., Kasvi, E., Hyyppä, H., and Alho, P.: Seamless mapping of river channels at high resoloution using mobile LiDAR and UAV photography, Remote Sensing, 5, 6382–6407, 2013.

Fonstad, M. A., Dietrich, J. T., Courville, B. C., Jensen, J. L., and Carbonneau, P. E.: Topographic structure from motion: a new development in photogrammetric measurement, Earth Surf. Proc. Land, 38, 421–430, 2013.

Francioni, M., Salvini, R., Stead, D., Giovanni, R., Riccucci, S., Vanneschi, C., and Gulli, D.: An integrated remote sensing-GIS approach for the analysis o fan open pit in the Carrara marble district, Italy: Slope stability assessment through kinematic and numerical methods, Comput. Geotech., 67, 46–63, 2015.

Giusti, F.: La storia naturale della Toscana Meridionale, Monte dei Paschi di Siena, Siena, Italy, 1993.

Haas, F.: Fluviale Hangprozesse in Alpinen Einzugsgebieten der Nördlichen Kalkalpen – Quantifizierung und Modellierungsansätze (Fluvial slope processes in alpine catchments of the northern calcareous alps – quantification and modelling approaches), Eichstätter Geographische Arbeiten, Vol. 17, Munich/Vienna, Germany/Austria, 2008.

Haas, F., Heckmann, T., Becht, M., and Cyffka, B.: Ground-based laserscanning a new method for measuring fluvial erosion on steep slopes. In GRACE, remote sensing and ground-based methods in multi-scale hydrology: Proceedings of the symposium JHS01 [entitled: GRACE, remote sensing and ground-based methods in multi-scale hydrology] held during the IUGG GA, Melbourne, Australia, 28 June–7 July 2011, 163–168, 2011.

Haas, F., Heckmann, T., Wichmann, V., and Becht, M.: Runout analysis of a large rockfall in the Dolomites/Italian Alps using LIDAR derived particle sizes and shapes, Earth Surf. Proc. Land., 37, 1444–1455, 2012.

Hancock, G. R., Crawter, D., Fityus, G., Chandler, J., and T. Wells: The measurement and modelling of rill erosion at angle of repose slopes in mine spoil, Earth Surf. Proc. Land., 33, 1006–11020, 2008.

Hancock, G. R., Lowry, J. B. C., and Coulthard, T. J.: Catchment reconstruction – erosional stability at millennial time scales using landscape evolution models, Geomorphology, 231, 15–27, 2015.

James, M. R. and Robson S.: Straightforward reconstruction of 3-D surfaces and topography with a camera: Accuracy and geoscience application, J. Geophys. Res., 117, F03036, doi:10.1029/2011JF002143, 2012.

James, R. J and Robson, S.: Mitigating systematic error in topographic models derived from UAV and ground-based image networks, Earth Surf. Proc. Land., 39, 1413–1420, 2014.

Kaiser, A., Neugirg, F., Rock, G., Müller, C., Haas, F., Ries, J., and Schmidt, J.: Small-Scale Surface Reconstruction and Volume Calculation of Soil Erosion in Complex Moroccan Gully Morphology Using Structure from Motion, Remote Sensing, 6, 7050–7080, 2014.

Lane, S. N., Westaway, R. M., and Murray H. D.: Estimation of erosion and deposition volumes in a large, gravel-bed, braided river using synoptic remote sensing, Earth Surf. Proc. Land., 28, 249–271, 2003.

Lindner, W.: Digital Photogrammetry, a practical course, Berlin, Heidelberg, Germany, 2009.

Martín-Duque, J. F., Sanz, M. A., Bodoque, J. M., Lucía, A., and Martín-Moreno, C.: Restoring earth surface processes trough landform design: a 13-year monitoring of a geomorphic reclamation model for quarries on slopes, Earth Surf. Proc. Land, 35, 531–548, 2010.

Mascaro, I., Benvenuti, M., Corsini, F., Costagliola, P., Lattanzi, P., Parrini, P., and Tanelli, G.: Minewastes at the polymetallic deposit of Fenice Capanne (southern Tuscany, Italy), Mineralogy, geochemistry and environmental impact, Environ. Geol., 41, 417–429, 2001.

Mathys, N., Klotz, S., Esteves, M., Descroix, L., and Lapetit, L. M.: Runoff and erosion in the Black Marls of the French Alps: Observations and measurements at the plot scale, Catena, 63, 261–281, 2005.

Moore, I. D., Grayson, R. B., and Ladson, A. R.:Digital terrain modelling: a review of hydrogical, geomorphological, and biological applications, Hydrol. Process., 5, 3–30, 1991.

Mossa, J. and James, L. A.: Impacts of mining on geomorphic systems, in: Treatise on Geomorphology, edited by: Shroder, J., San Diego, CA, USA, 74–95, 2013.

Neugirg, F., Kaiser, A., Schmidt, J., Becht, M., and F. Haas: Quantification, analysis and modelling of soil erosion on steep slopes using LiDAR and UAV photographs. In sediment dynamics from the summit to the sea, (Proceedings of a symposium held in New Orleans, Louisiana, USA, 11–14 December 2014), IAHS Publ., 367, 51–58, 2014.

Neugirg, F., Kaiser, A., Huber, A. C., Heckmann, T., Schindewolf, M., Schmidt, J., Becht, M., and Haas, F.: Using terrestrial LiDAR data to analyse morphodynamics on steep unvegetated slopes

driven by different geomorphic processes, Catena, 142, 269–280, 2016.

Nowotny, V.: Water Quality – Diffuse Pollution and Watershed Management, Hoboken, New Jersey, USA, 598 pp., 2003.

Osterkamp, W. R. and Joseph, W. L.: Climatic and hydrologic factors associated with reclamation, in: Reclamation of Drastically Disturbed Lands, edited by: Barnishe, I. R., Darmody, R., and Daniels, W., American Society of Agronomy, Madison, WI, USA, 193–216, 2000.

Ouédraogo, M. M., Degré, A., Debouche, C., and Lisein, J.: The evaluation of unmanned aerial systems-based photogrammetry and terrestrial laser scanning to generate DEMs of agricultural watersheds, Geomorphology, 214, 339–355, 2014.

Peter, K. D., d'Oleire-Oltmanns, S., Ries, J. B., Marzolff, I., and Ait Hssaine, A.: Soil erosion in gully catchments affected by land-levelling measures in the Souss Basin, Morocco, analyzed by rainfall simulation and UAV remote sensing data, Catena, 113, 24–40, 2014.

Prosdocimi, M., Calligaro, S., Sofia, G., Dalla Fontana, G., and P. Tarolli: Bank erosion in agricultural drainage networks: new challenges from structure-from-motion photogrammetry for post-event analysis, Earth Surf. Proc. Land, 40, 1891–1906, 2015.

Quinn, P. F., Beven, K. J., Chevallier, P., and Planchon, O.: The prediction of hillslope flow paths for distributed hydrological modelling using digital terrain models, Hydrol. Process., 5, 59–79, 1991.

Schürch, P., Densmore, A. L., Rosser, N. J., Lim, M., and McArdell, B. W.: Detection of surface change in complex topography using terrestrial laser scanning: application to the Illgraben debris-flow channel, Earth Surf. Proc. Land., 36, 1847–1859, 2011.

Servida, D., Grieco, G., and De Capitani, L.: Geochemical hazard evaluation of sulphide-rich iron mines: The Rio Marina district, J. Geochem. Explor., 100, 75–89, 2009.

Smith, M. W. and Vericat, D.: From experimental plots to experimental landscapes: topography, erosion and deposition in sub-humid badlands from Structure-from-Motion photogrammetry, Earth Surf. Proc. Land, 40, 1656–1671, 2015.

Sperlich, M., Kattenborn, T., Koch, B., and Kattenborn, G.: Potential of unmanned aerial vehicle based photogrammetric point clouds for automatic single tree detection, DGPF Tagungsband, 23, 2014.

Tarolli, P.: High-resolution topography for understanding Earth surface processes: Opportunities and challenges, Geomorphology, 216, 295–312, 2014.

Taylor, J. R.: An introduction to error analysis, The study of uncertainties in physical measurements, Sausalito, CA, USA, 1997.

Westaway, R. M., Lane, S. N., and Hicks, D. M.: The development of an automated correction procedure for digital photogrammetry for the study of wide, shallow, gravel bed rivers, Earth Surf. Proc. Land., 25, 209–226, 2000.

Wetzel, K.-F.: Abtragsprozesse an Hängen und Feststoffführung der Gewässer. Dargestellt am Beispiel der pleistozänen Lockergesteine des Lainbachgebietes – Benediktbeuern/ Obb. (Erosion processes on slopes and sediment transport of channels. A case study of Pleistocene sediment depots of the Lainbach – valley Benediktbeuern/Bavaria, Münchener geographische Abhandlungen, Vol. B17, Munich, Germany, 1992.

Ying Yang, M. and Förstner, W.: Plane Detection in Point Cloud Data. Department of Photogrammetry, Institute of Geodesy and Geoinformationm University of Bonn. Bonn (Technical Report, 1), available at: https://drive.google.com/file/d/0B4ZTx-3R0B29NHdSQk9SMDdtUU0/view?pref=2&pli=1 (last access: 30 May 2016), 2010.

Zevenbergen L. W. and Thorne C. R.: Quantitative analysis of land surface topography, Earth Surf. Proc. Land., 12, 47–56, 1987.